

High-energy emission from tidal disruption events in active galactic nuclei

Chi-Ho Chan^{1,2}, Tsvi Piran¹, and Julian H. Krolik³

¹Racah Institute of Physics, Hebrew University of Jerusalem, Jerusalem 91904, Israel

²School of Physics and Astronomy, Tel Aviv University, Tel Aviv 69978, Israel

³Department of Physics and Astronomy, Johns Hopkins University, Baltimore, MD 21218, USA

April 29, 2021

ABSTRACT

Tidal disruption events (TDEs) taking place in active galactic nuclei (AGNs) are different from ordinary TDEs. In these events, the returning tidal debris stream drills through the pre-existing AGN accretion disk near the stream pericenter, destroying the inner disk in the process, and then intersects with the disk a second time at radii ranging from a few to hundreds of times the pericenter distance. The debris dynamics of such TDEs, and hence their appearance, are distinct from ordinary TDEs. Here we explore the observational signatures of this “second impact” of the stream with the disk. Strong shocks form as the dilute stream is stopped by the denser disk. Compton cooling of the shocked material produces hard X-rays, even soft γ -rays, with most of the energy emitted between ~ 10 keV and 1 MeV. The luminosity follows the mass-return rate, peaking between $\sim 10^{42}$ and 10^{44} erg s⁻¹. The X-ray hardness and the smoothness of the light curve provide possible means for distinguishing the second impact from ordinary AGN flares, which exhibit softer spectra and more irregular light curves.

Key words: galaxies: nuclei – accretion, accretion disks – black hole physics – hydrodynamics

1. INTRODUCTION

Supermassive black holes at galactic centers can generate copious amounts of radiation. When a black hole is fed a steady diet of gas from galactic scales, the gas forms an accretion disk around the black hole, and the black hole manifests itself as an active galactic nucleus (AGN) that shines across the entire electromagnetic spectrum. The luminosity of an AGN varies over time, exhibiting variations from mundane, $\sim 10\%$ fluctuations to more dramatic flares.

Once in a while, a star in the nuclear cluster of the host galaxy may be scattered onto an orbit grazing the black hole. A tidal disruption event (TDE) takes place when the tidal gravity of the black hole overwhelms the self-gravity of the star and breaks the star apart (Hills 1975). Energy redistribution during the disruption leaves roughly half of the star gravitationally bound to the black hole while unbinding the other half (e.g., Rees 1988). If the black hole is not surrounded by a disk, the bound debris returns to the neighborhood of the black hole as an elongated stream, shocks against itself, and settles into an accretion flow that emits primarily in the optical/ultraviolet (UV). The unbound debris produces synchrotron radiation through its interaction with the circumnuclear medium (Krolik et al. 2016; Yalinewich et al. 2019).

If the disruption takes place in an AGN with a pre-existing disk, the system initially evolves almost as if the disk were absent. Because one large-angle two-body scattering in the nuclear star cluster suffices to reduce a star’s pericenter to within the tidal radius, a typical star does not pass through the small-scale disk multiple times before disruption (MacLeod & Lin 2020). The mutual influence between the star and the disk in a single transit is extremely limited: the internal structure of the star is barely altered (Syer et al. 1991; Miralda-Escudé & Kollmeier 2005); the compact star scarcely opens a gap in the disk (Suková et al. 2021); and hydrodynamic drag hardly changes the stellar orbit

(Syer et al. 1991; Rauch 1995; Miralda-Escudé & Kollmeier 2005; Just et al. 2012). This means both the star and the disk are fully intact before the disruption, and the star’s trajectory is independent of the disk’s orientation. The disruption itself is also unaffected by the disk, due to the much higher density of the star and the debris.

The story after the debris stream falls back to pericenter is strongly modified because the debris at this point is much more dilute. The most vigorous interaction between stellar and disk material happens when the stream makes first contact with the disk. Stream fallback and disk rotation carry comparable mass currents (Chan et al. 2019; see also Kochanek 1994), and the stream is also geometrically extended; both properties are critical for stream impact to significantly reshape the disk. At the same time, the presence of the disk impedes stream self-intersection, so the observational signatures of a TDE in an AGN may not resemble one in vacuum at all.

In addition to their possibly different appearance, the challenge of finding TDEs in AGNs is compounded by the fact that AGNs exhibit frequent flares. Strategies for separating out TDEs usually depend on light-curve timescales and optical colors (e.g., van Velzen et al. 2021), but the nature of any one event is often disputed (Komossa 2015; Kankare et al. 2017; Auchettl et al. 2018; Trakhtenbrot et al. 2019; Frederick et al. 2020). This underlines the importance of understanding how TDEs in AGNs produce their light.

We were the first to explore the hydrodynamic and radiative properties of TDEs in AGNs (Chan et al. 2019, 2020). We call the pericentric collision of the returning stream with the disk the *first impact*. An important quantity to consider is the disk mass interior to the impact point. For example, for a black hole of mass $M_h = 3 \times 10^6 M_\odot$ and a Sun-like star, the physical tidal radius \mathcal{R}_t , or the maximum pericenter for total disruption, is $\sim 12 r_g$ (Ryu et al. 2020a), where $r_g \equiv GM_h/c^2$ is the gravitational

radius. A Shakura & Sunyaev (1973) disk accreting at 0.01 times Eddington has a meager $\sim 10^{-4} M_{\odot}$ inside this radius. It follows immediately that the first impact can significantly reshape the inner disk.

This expectation is confirmed by the hydrodynamics simulations in Chan et al. (2019). Shocks emanating from the first impact dissipate energy and remove angular momentum so vigorously that they vacate the inner disk within tens of days. The dissipated energy keeps the bolometric luminosity constant at Eddington levels for a similar amount of time (Chan et al. 2020). Unfortunately, the complicated hydrodynamic and radiative environment of the inner disk prevents us from estimating first-impact spectra without detailed simulations and radiative-transfer calculations.

There is, however, another way by which TDEs in AGNs can glow. Most streams have enough inertia to punch through the disk, all the more so after shocks have gotten rid of the inner disk. As illustrated in Figure 1, the stream, tidally compressed during its pericenter passage and ruffled by the first impact, spews out fan-shaped from the other side. As we shall see later, stream material can be sprayed as far as ~ 100 times the pericenter distance, and when it finally meets the disk again, it is much more dilute than the disk it lands on. The relation between stream mass and disk mass is also very different: for the example above, the disk within $\sim 100 R_t$ contains $\sim 17 M_{\odot}$. Even though the disk does not carry much more mass than the stream, it is still much denser, mostly because all that mass is concentrated within a small scale height. Because of the density disparity, the stream is likely absorbed in its entirety by the disk without altering the disk to any appreciable extent.

The energy dissipated at this *second impact* powers another flare, on top of that from the first impact. Different circumstances suggest different observational signatures; specifically, the simpler geometry of the second impact allows us to more easily model the cooling process and compute the spectrum.

We begin by accentuating in §2 the dissimilar nature of TDEs in vacuum and TDEs in AGNs. Our investigation of the second impact begins in §3 with a survey of system parameters. The dynamical and energetic aspects of the second impact are addressed in §4. The core of our exposition is §5, where we translate the energy dissipation rates from the previous section to spectra using a simple Compton-cooling model. A discussion of the results is found in §6, followed by our conclusions in §7.

2. TDES IN AGNS AS A DISTINCT POPULATION FROM TDES IN VACUUM

A primary point of contention about TDEs in vacuum is whether shocks can transform the eccentric stream to a more circular accretion flow and, if so, how. In the classical picture, general-relativistic apsidal precession makes the stream self-intersect near pericenter; the resulting strong shocks dissipate energy briskly, forcing the stream to circularize and settle into a compact accretion disk (e.g., Rees 1988). The radiation from this disk might be reprocessed by surrounding optically thick matter (e.g., Loeb & Ulmer 1997; Metzger & Stone 2016; Lu & Bonnerot 2020; but see Matsumoto & Piran 2021). However, if the disruption takes place at $\geq 10 r_g$, precession leads instead to shocks that are closer to apocenter (Shiokawa et al. 2015; Dai et al. 2015). These apocentric shocks are the result of the stream

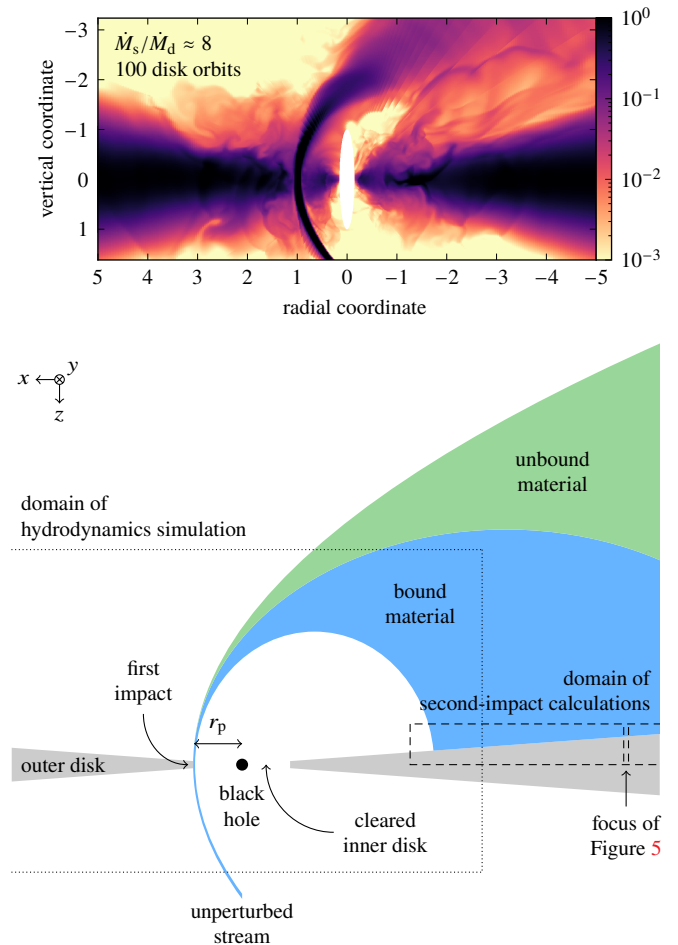


Figure 1. Interaction of a TDE stream with an AGN disk. *Top panel:* Density slice of one of the hydrodynamics simulations this work is based upon, set up according to Chan et al. (2019). The slice is rotated upside-down in anticipation of §5.1. The white ellipse around the origin is due to the numerical cutout, whose purpose is to exclude the cylindrical axis from the simulation domain. The stream penetrates the disk at the first impact. Shocks excited there nearly evacuate the disk interior to the impact point. Subjected to tidal compression during its pericenter passage, internal pressure forces widen the stream on exit from the disk. *Bottom panel:* Schematic diagram of the framework employed to calculate the properties of the second impact. Pressure forces internal to the stream widen its energy distribution. Most of the stream material is gravitationally unbound, and the rest is dispersed over a large swath of the outer disk. The much lower density of the stream at this second impact means it can be completely absorbed by the disk. The skinny dashed box picks out an arbitrary annulus of the disk; Figure 5 shows the detailed structure of the region inside the box.

interacting with the complex, eccentric accretion flow created by earlier-returning tidal debris. They are too weak to efficiently circularize the stream, but they can generate optical/UV light (Piran et al. 2015).

The picture is fundamentally different for TDEs in AGNs. The obstruction posed by the disk means the stream cannot in general self-intersect; specifically, the first impact prevents rapid circularization, while the second impact precludes apocentric shocks. Mechanisms discussed in the context of TDEs in vacuum, including reprocessing and apocentric shocks as the origin of optical/UV emission, are therefore wholly inapplicable to TDEs in AGNs.

The physics of TDEs in AGNs must be studied in its own right.

The most energetic stream–disk interaction comes about when the stream first returns to pericenter, at the first impact. Shocks excited by the impact accelerate inflow in the inner disk, which leads to vigorous energy dissipation, often super-Eddington in power (Chan et al. 2019). The bolometric luminosity depends on a balance between energy dissipation, radiation diffusion, and photon trapping (Chan et al. 2020). These mechanisms operate in qualitatively the same way no matter how close the stream approaches to the black hole, or how much apsidal precession it suffers on its pericentric flyby. The second impact, the focus of this article, happens when the stream is arrested near its apocenter as it flies over the disk. As expanded upon in §5.4, the second-impact shocks likely emit primarily hard X-rays to soft γ -rays.

Even the energy reservoir is different for the two kinds of TDEs. For TDEs in vacuum, the energy radiated by the bound debris must ultimately be sourced from its orbital energy. By contrast, TDEs in AGNs can tap into the orbital energy of the disk as well. In most TDEs of the latter kind, the returning debris plays the role of a catalyst, causing orbital energy to be liberated at much higher rates than in the unperturbed disk. This statement is true for the first impact, whose near-Eddington luminosity results from the speedy infall of the inner disk (Chan et al. 2019, 2020). It is also true for the second impact: we shall see in §4.2 that stream material dissipates the kinetic energy of the part of the disk it lands on, at a rate proportional to its mass current.

Thus, *TDEs in vacuum and TDEs in AGNs have entirely distinct appearances*. Searches tailored to one type may be insensitive to the other. To find TDEs in AGNs, a completely new set of distinguishing features must be constructed for this novel class of transients. In addition, there is a second difficulty: winnowing away the cases in which “flares” are merely intrinsic AGN variability.

3. PARAMETERS

We consider the case where the pericenter distance r_p of the debris stream equals the physical tidal radius \mathcal{R}_t , the maximum pericenter for complete disruption. This radius is a function of the black-hole mass M_h and the stellar mass M_\star . Both \mathcal{R}_t and the peak rate \dot{M}_s at which bound tidal debris returns to pericenter are given by the following expressions, derived from general-relativistic hydrodynamics simulations of the disruption of stars with realistic internal structure (Ryu et al. 2020a):

$$\mathcal{R}_t \approx 1.0 \times 10^{13} \text{ cm} \times \Psi \left(\frac{M_h}{3 \times 10^6 M_\odot} \right)^{1/3} \left(\frac{M_\star}{M_\odot} \right)^{-1/3} \left(\frac{r_\star}{r_\odot} \right), \quad (1)$$

$$\dot{M}_s \approx 1.7 M_\odot \text{ yr}^{-1} \times \Xi^{3/2} \left(\frac{M_h}{3 \times 10^6 M_\odot} \right)^{-1/2} \left(\frac{M_\star}{M_\odot} \right)^2 \left(\frac{r_\star}{r_\odot} \right)^{-3/2}. \quad (2)$$

Unlike Ryu et al. (2020a), here we use $3 \times 10^6 M_\odot$ as our fiducial M_h . In these equations,

$$r_\star \approx 0.93 r_\odot \times \left(\frac{M_\star}{M_\odot} \right)^{0.88} \quad (3)$$

is the stellar radius (Ryu et al. 2020b), and the dimensionless factors

$$\Psi(M_h, M_\star) \equiv \{0.80 + 0.45 [M_h / (3 \times 10^6 M_\odot)]^{0.50}\} \times \frac{1.47 + \exp((M_\star/M_\odot - 0.67)/0.14)}{1 + 2.34 \exp((M_\star/M_\odot - 0.67)/0.14)}, \quad (4)$$

$$\Xi(M_h, M_\star) \equiv \{1.27 - 0.21 [M_h / (3 \times 10^6 M_\odot)]^{0.24}\} \times \frac{0.62 + \exp((M_\star/M_\odot - 0.67)/0.21)}{1 + 0.55 \exp((M_\star/M_\odot - 0.67)/0.21)} \quad (5)$$

refine earlier order-of-magnitude estimates (e.g., Rees 1988). For $M_h = 3 \times 10^6 M_\odot$ and $M_\star = M_\odot$, the revised r_p is $\approx 12 r_g$, roughly half the value used in Chan et al. (2019, 2020). This changes the dependence of timescales and stream mass current on TDE parameters.

In our previous work, we investigated the interaction of the stream with the disk at the first impact using a suite of Newtonian hydrodynamics simulations (Chan et al. 2019). In those simulations, a disk was set up along the midplane, and a stream on a parabolic orbit was injected from above in such a way that it made perpendicular contact with the disk exactly when it reached pericenter. Because the simulations lasted only a fraction of the mass-return time, the stream mass current was kept constant at \dot{M}_s . The same simulation setup is employed to study the second impact.

The chief parameter characterizing both impacts is \dot{M}_s/\dot{M}_d , where \dot{M}_d is the mass current of the unperturbed disk rotating under the stream footprint at the first impact. Assuming a Shakura & Sunyaev (1973) disk, we found that \dot{M}_s/\dot{M}_d has a minimum, and $\dot{M}_s/\dot{M}_d \gtrsim 1$ for reasonable TDE and AGN parameters (Chan et al. 2019); therefore, we consider here $\dot{M}_s/\dot{M}_d \in \{\approx 4, \approx 8, \approx 16, \approx 32\}$, which are typical for TDEs in AGNs. The last three values of \dot{M}_s/\dot{M}_d necessitate new runs not reported in Chan et al. (2019).

We characterize the AGN in terms of its unperturbed disk luminosity $\eta \dot{M}_d c^2$, where $\eta = 0.1$ is the fiducial accretion efficiency. Every value of \dot{M}_s/\dot{M}_d above the minimum corresponds to two values of \dot{M}_d , the larger and smaller values appropriate for a disk whose pressure is dominated by radiation and gas, respectively (Chan et al. 2019). We adopt the larger value here.

4. SECOND IMPACT

4.1. Trajectory calculations

Figure 1 combines a density slice from the actual simulations with a schematic depiction of the bigger picture. A stream with $\dot{M}_s/\dot{M}_d \gtrsim 1$ punches through the disk at the first impact. Tidal compression redistributes energy within the stream; as a result, a dilute, wide-angle plume of stream material bursts out from the lower side of the disk. Our focus is on the fraction that returns to the disk.

Because stream material leaves the simulation domain with sound speeds much less than virial, $\lesssim 0.1 [GM_h/(R^2+z^2)]^{1/2}]^{1/2}$ (Chan et al. 2019), we assume it follows ballistic trajectories from the boundaries of the simulation domain until they strike the disk. For each time step in each run, we determine which boundary cells have outflowing gas with specific angular momentum $\geq 1.1 (GM_h r_p)^{1/2}$ in the y -direction; these cells have outflowing stream material, as opposed to vertically expanding disk gas.

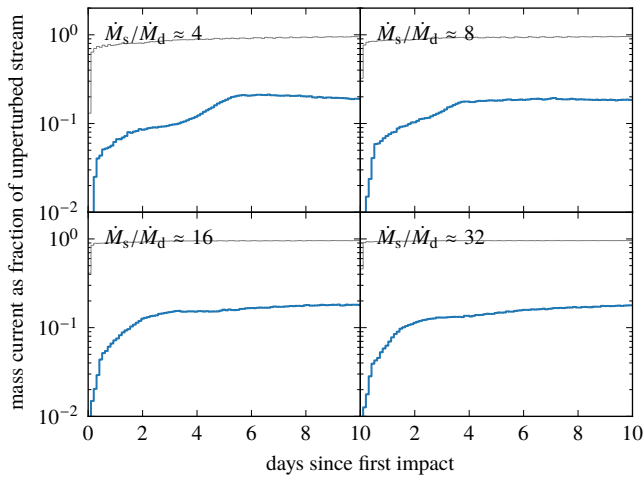


Figure 2. Rate at which stream material leaves the simulation domain as a thin curve, and rate at which it falls back to the midplane as a thick curve, for $M_h = 3 \times 10^6 M_\odot$ and $M_\star = M_\odot$. All rates are normalized by the unperturbed stream mass current \dot{M}_s .

For each of these cells, we assume that all the outflowing material over the time step is launched outward on a Keplerian trajectory. We calculate when, where, and with what velocity this trajectory hits the midplane. Even gravitationally unbound gas can be intercepted if its hyperbolic trajectory crosses the disk. Trajectory calculations are continued until the end of the simulations, at time $1400 (GM_h/r_p^3)^{-1/2}$, which is more than double the simulation duration in Chan et al. (2019); for $M_h = 3 \times 10^6 M_\odot$ and $M_\star = M_\odot$, this translates to ~ 10 d, or about a quarter of the orbital period of the most bound debris when these parameters apply. The mass fallback rate as a function of time is a convolution of the outflow rate and the flight-time delay.

4.2. Dynamics and energetics

Figure 2 contrasts the rate at which stream material crashes back to the disk as a function of time with the rate at which it exits the first-impact region. Most of the material is unbound, and only $\sim 20\%$ is involved in the second impact.

Figure 3 is a map of where the material lands on the disk over the course of the simulation, and the left panel of Figure 4 displays the azimuthally integrated mass fallback rate. The trajectories followed by the bulk of the material from the first impact to the second have eccentricities ≈ 1 , and the planes of the trajectories are almost perpendicular to the disk. These trajectories dump the material along the projection of the unperturbed stream onto the disk. A tiny portion of the material is heavily deflected and put on mildly eccentric, highly inclined trajectories with a range of orientations; this material ends up at $r \lesssim 3 r_p$. Although the detailed shape of the splash zone and the rate at which material is delivered to it vary with time and \dot{M}_s/\dot{M}_d , overall they are remarkably independent of these two variables. This means the properties of the second impact depend less on AGN properties (\dot{M}_d) and more on TDE properties (M_h, M_\star).

The right panel of Figure 4 shows the azimuthally integrated

energy dissipation rate per logarithmic radius:

$$R^2 \int d\phi \rho_f v_{f,z} K, \quad (6)$$

where ρ_f and \mathbf{v}_f are the density and velocity of the material falling back, $K \equiv \frac{1}{2} \|\mathbf{v}_f - R\Omega \hat{\mathbf{e}}_\phi\|^2$ is the specific energy dissipation rate, $\Omega = (GM_h/R^3)^{1/2}$ is the Keplerian orbital frequency, and the integral is over where the material hits. At radii greater than a few r_p , material hits the disk with $\|\mathbf{v}_f\| \ll R\Omega$; as a result, the dissipated energy is mainly derived from the kinetic energy of the disk, that is, $K \propto 1/R$. At all radii, the energy dissipation rate due to the second impact is orders of magnitude greater than that of the underlying disk; in fact, the energy dissipated per orbital time can reach $\sim 10^{-3}$ times the local binding energy at certain radii. The expedited inflow this entails could help feed the small-scale disk emptied by the shocks from the first impact (Chan et al. 2019).

The spatial distribution and energy dissipation of the second impact depend on the strength of the pericentric tidal compression. This in turn depends on the kinematic properties of the unperturbed stream, which cannot be accurately determined without simulating the full disruption process. Therefore, the results presented here should be understood as capturing the qualitative, not quantitative, aspects of the second impact.

5. COMPTON COOLING

The next step is to estimate the photon energies at which the dissipated energy is radiated from the disk. The task is non-trivial because, at the same time the stream material shocks and dissipates its energy, its internal energy is converted to radiation through Compton cooling and carried away with the escaping radiation. Here we construct a crude model that captures the essence of these concurrent processes; characterization of the potentially radiation-dominated shocks and detailed spectral calculations are left to future work.

5.1. Overall picture

Figure 5 shows an idealized picture of the second impact in the inertial frame. Falling stream material is slowed down, compressed, and heated by a strong, standing reverse shock. The layer of shocked material, sitting on the disk, is ferried away by disk rotation. This material cools quite swiftly; with the loss of pressure support, presumably it sinks into the disk within one orbit. As is evident from the narrowness of the splash zones displayed in Figure 3, the time for the disk to rotate through the stream is much shorter than an orbital period. The structure in Figure 5 is thus time-steady: the unperturbed disk enters from the left side, and exits to the right topped with cooled shocked material.

Over longer timescales, this time-steady picture changes gradually as the rate at which stream material descends on the disk varies. The mass current of the second impact slowly builds up in the early stages of the TDE because the stream takes time to fly from the first impact to the second. In addition, on timescales comparable to the mass-return time of the TDE, the rate at which stellar material returns to pericenter declines, and so does the mass current going to the second impact.

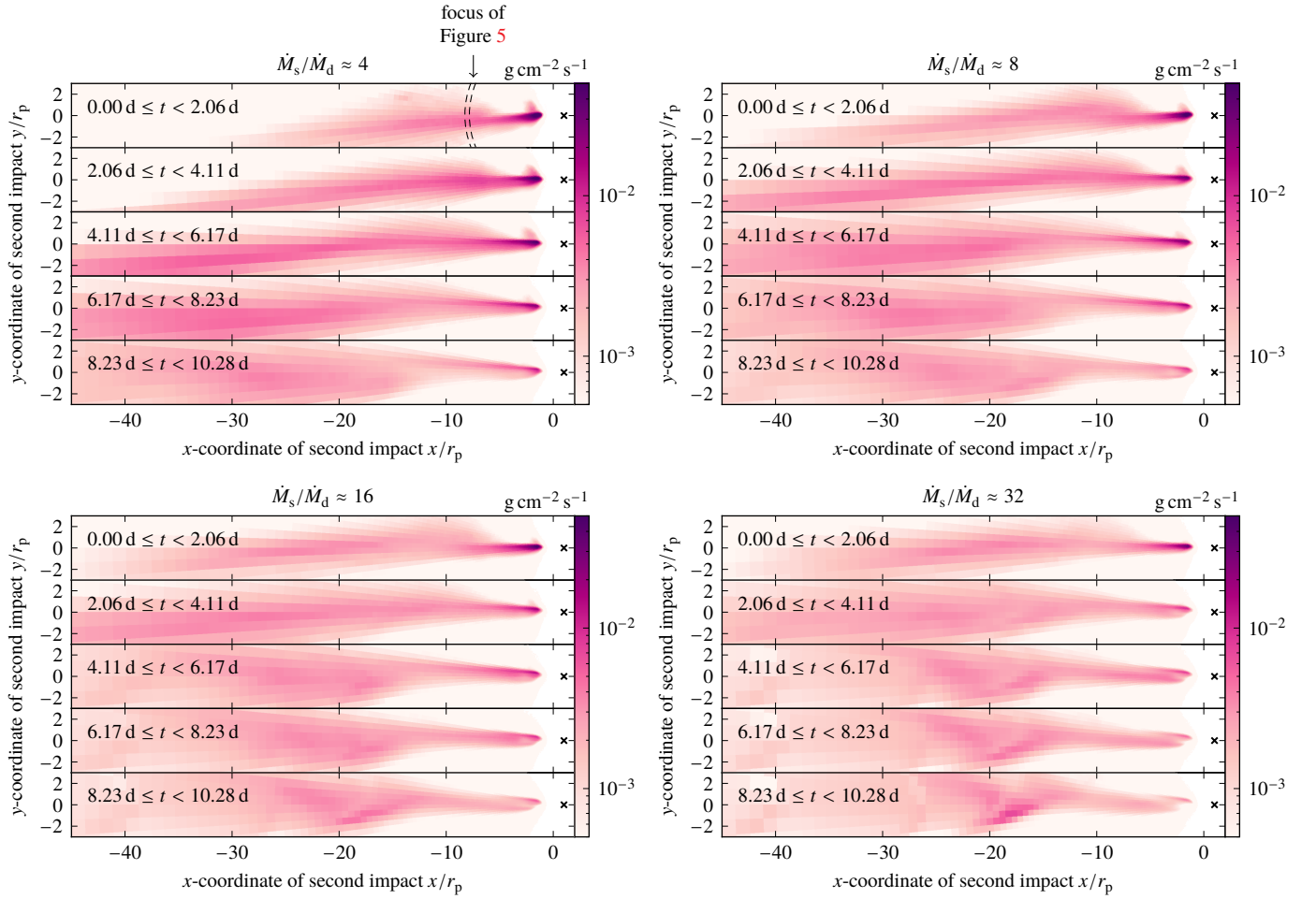


Figure 3. Flux of stream material falling back to the midplane for $M_{\text{h}} = 3 \times 10^6 M_{\odot}$ and $M_{\star} = M_{\odot}$. The flux is the time integral of mass landing in a cell over one of the five intervals indicated in each panel, divided by the area of the cell and the length of the interval. The black hole is at the origin, and the cross marks the first impact. Figure 5 shows how the second impact along an arbitrary annulus of the disk, such as the dashed one in the top-left panel, looks like as viewed from the black hole.

Our simulations, which last for ~ 10 d when $M_{\text{h}} = 3 \times 10^6 M_{\odot}$ and $M_{\star} = M_{\odot}$, are long enough to cover only the buildup period. To study how the second impact changes over this period, we divide the simulation duration into five equal intervals. The fall-back material is characterized by its speed, mass flux, and energy dissipation rate; for simplicity, we assume these three quantities are time-independent within each interval and ϕ -independent across the stream, so we can consider their averages $\langle v_{f,z} \rangle$, $\langle \rho_f v_{f,z} \rangle$, and $\langle \rho_f v_{f,z} K \rangle$.

5.2. Cooling model

To calculate the cooling emission, we follow a point on the disk at radius R from the moment it enters the stream, which we take to be $t = 0$. A column of shocked material accumulates above the point as it moves through the stream; meanwhile, the column cools by radiating away the dissipated energy. The point leaves the stream at $t_{\text{dep}} = \Delta\phi/\Omega$, where $\Delta\phi$ is the characteristic azimuthal width of the second impact at radius R ; we nevertheless continue tracking the cooling over the entire orbit to ensure the column has largely cooled off by the time it returns to the stream. The observed cooling emission is the sum from columns all over the disk, each in a different cooling stage.

The dominant cooling mechanism is inverse Compton scattering of seed photons from the disk. In this sense, the shocked layer behaves similarly to an AGN corona (e.g., Haardt & Maraschi 1991), except that the shocked layer can be quite Compton-thick. Synchrotron emission should not contribute greatly because it is strongly self-absorbed, and we shall see later that free-free cooling is also unlikely to be important.

We assume the shocked layer is vertically homogeneous, and ions and electrons are thermal at the same temperature. Thermal electrons at the temperatures we find are mildly relativistic; therefore, we ignore electron-positron pair production and the Klein-Nishina reduction in cross section, both affecting only a small fraction of photons.

The spectrum of the Comptonized photons is taken to be a power law with a cutoff. Seed photons from the disk carry a radiative flux

$$F_{\text{d}} = \frac{3GM_{\text{h}}\dot{M}_{\text{a}}}{8\pi R^3}, \quad (7)$$

and their spectrum is black-body at temperature $T_{\text{d}} = (F_{\text{d}}/\sigma_{\text{SB}})^{1/4}$, where σ_{SB} is the Stefan-Boltzmann constant. Because the seed spectrum is much narrower than the Comptonized spectrum, we approximate the former as a delta function. We use F_{d} of the unperturbed disk here, but spiral shocks extending

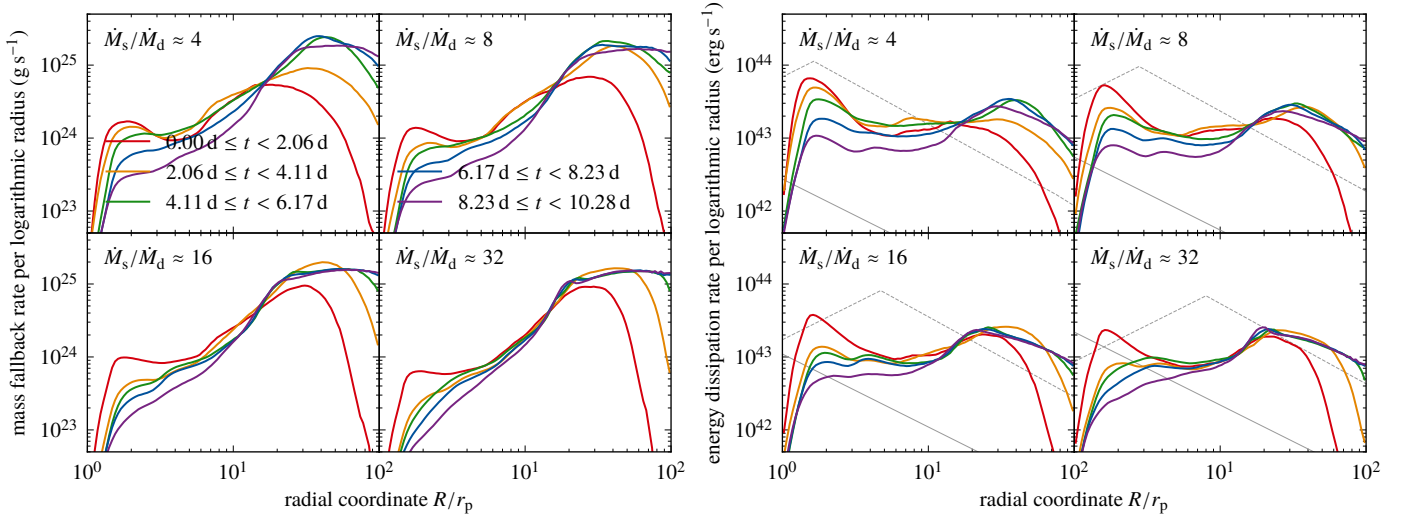


Figure 4. *Left panel:* Mass fallback rate per logarithmic radius at the second impact for $M_h = 3 \times 10^6 M_\odot$ and $M_\star = M_\odot$. The legend applies to the right panel as well. *Right panel:* Energy dissipation rate per logarithmic radius as given by Equation (6), for the same M_h and M_\star . The thin solid line is 10 times the energy dissipation rate per logarithmic radius of the underlying disk. The thin dashed line is 10^{-3} times the binding energy per logarithmic radius of the disk divided by the orbital time; the break in this line is at the radius where disk pressure changes from radiation-dominated on the inside to gas-dominated on the outside.

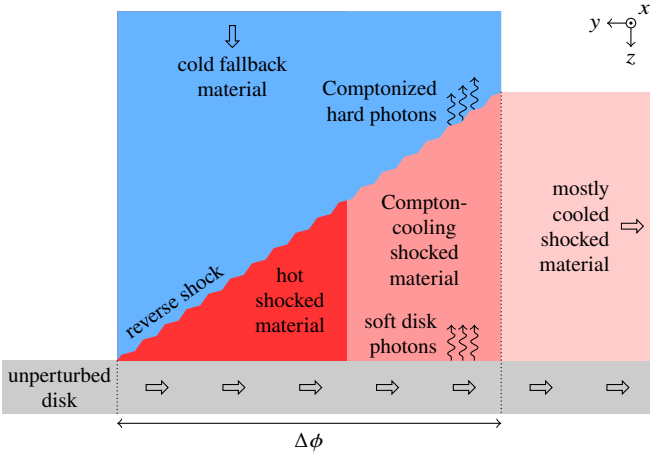


Figure 5. Schematic diagram of the second impact. This figure shows how the skinny dashed box in Figure 1 or the dashed annulus in Figure 3 looks from the perspective of the black hole; colors represent in an approximate manner the different physical states of the gas. The unperturbed disk (gray) moves in from the left. Cold stream material (blue) falls inelastically onto the disk and is constantly transported to the right by disk rotation. The standing, oblique reverse shock thus formed heats the material (dark red). At the same time, soft seed photons from the disk undergo inverse Compton scattering and harden as they propagate upward through the shocked material. Compton cooling is efficient only in parts of the material (light red) that are somewhat Compton-thick in the vertical direction. This mostly cooled material (pale red) likely sinks into the disk over the course of an orbit, so that the disk rotates back into the stream in its unperturbed state.

outward from the first impact (Chan et al. 2019) could modify the disk and thus F_d .

At each moment, the model is characterized by E_g and E_r , which are, respectively, the vertically integrated gas and radiation energy densities; by E_∞ , the energy per area that has escaped from the top of the column; and by H_{sh} , the height of the column

of shocked material. They obey the equations

$$\frac{dE_g}{dt} = \langle \rho_f v_{f,z} K \rangle \vartheta(t_{dep} - t) - (A - 4\Theta_C) \frac{E_r}{t_{sca}}, \quad (8)$$

$$\frac{dE_r}{dt} = F_d + (A - 4\Theta_C) \frac{E_r}{t_{sca}} - \frac{E_r}{t_{esc}}, \quad (9)$$

$$\frac{dE_\infty}{dt} = \frac{E_r}{t_{esc}}, \quad (10)$$

$$\frac{dH_{sh}}{dt} = \begin{cases} v_{sh} & \text{if } t < t_{dep}, \\ (H_{eq}/H_{sh} - 1)c_s & \text{if } t \geq t_{dep}, \end{cases} \quad (11)$$

where ϑ is the step function, and the other symbols are defined in the rest of the section. The initial condition is $(E_g, E_r, E_\infty, H_{sh}) = (0, 0, 0, 0)$; the results are insensitive to small perturbations to the initial condition.

Equation (8) characterizes the accrual of dissipated energy in the column and its conversion to radiation through Compton scattering. Equation (9) follows the increase in radiation energy as a result of disk injection and Compton scattering, and its decrease due to radiative losses. Equation (11) describes how the column grows during deposition while mass and heat are added to it, and collapses after deposition as it cools. We ignore the internal energy increase during this collapse due to adiabatic compression and release of gravitational energy, both being secondary effects.

In Equations (8) and (9), A is the fractional photon energy gain due to inverse Compton scattering, and Θ_C is the Compton temperature in units of $m_e c^2 / k_B$, with m_e the electron mass and k_B the Boltzmann constant. The Compton temperature is the temperature of an electron gas in thermal balance with photons through Compton scattering, and it is equal to one-fourth the intensity-weighted mean photon energy.

Three timescales appear in the equations:

$$t_{dep} = \Delta\phi / \Omega, \quad (12)$$

$$t_{sca} = 1 / (n_e \sigma_T c), \quad (13)$$

$$t_{esc} = (H_{sh} / c) \max(1, \tau_T), \quad (14)$$

where n_e is the electron number density, σ_T is the Thomson cross section, and τ_T is the Thomson thickness. These timescales are, respectively, the duration of deposition, the mean timescale for a photon to scatter off an electron, and the timescale for radiation to escape. We also define

$$v_{\text{sh}} = [(\gamma - 1)/(\gamma + 1)] \langle v_{f,z} \rangle, \quad (15)$$

$$H_{\text{eq}}^2 = 2c_s^2 R^3 / (GM_{\text{h}}), \quad (16)$$

$$c_s^2 = (\frac{2}{3}E_g + \frac{1}{3}E_r) / \Sigma_{\text{sh}}, \quad (17)$$

$$n_e = \Sigma_{\text{sh}} / (2\bar{m}H_{\text{sh}}), \quad (18)$$

$$\tau_T = \sigma_T \Sigma_{\text{sh}} / m_{\text{H}}, \quad (19)$$

$$\Sigma_{\text{sh}} = \langle \rho_f v_{f,z} \rangle \min(t_{\text{dep}}, t). \quad (20)$$

Here v_{sh} is the upward speed of the reverse shock in the corotating frame, H_{eq} is the scale height in hydrostatic equilibrium, c_s is the isothermal sound speed, Σ_{sh} is the column density, $\gamma = \frac{5}{3}$ is the adiabatic index, $\bar{m} = \frac{8}{13}m_{\text{H}}$ is the mean particle mass, and m_{H} is the hydrogen mass.

Although the electrons are mildly relativistic at the beginning, the radiative output is dominated by later stages when the gas is cooler; we therefore have

$$A \approx 4\Theta, \quad (21)$$

where

$$\Theta \equiv k_{\text{B}}T_{\text{g}} / (m_e c^2), \quad (22)$$

and

$$T_{\text{g}} = (\gamma - 1)\bar{m}E_{\text{g}} / (k_{\text{B}}\Sigma_{\text{sh}}) \quad (23)$$

is the gas temperature.

We compute the Compton temperature in two different ways, distinguished by whether the column is Compton-thin or thick. The dividing line $\tau_T = 1/e$ is chosen to be as large as possible while being small enough that the probability of n scatters is $\approx \tau_T^n$. If $\tau_T < 1/e$, most disk photons escape without being scattered, so the spectrum of the radiation emerging from the column consists of a delta-function disk component in addition to a Comptonized component:

$$F(\epsilon) d\epsilon = \left[(1 - \tau_T)F_{\text{d}} \delta(\epsilon - k_{\text{B}}T_{\text{d}}) + \frac{F_{\text{C}}}{k_{\text{B}}T_{\text{g}}} \left(\frac{\epsilon}{k_{\text{B}}T_{\text{g}}} \right)^p \exp\left(-\frac{\epsilon}{k_{\text{B}}T_{\text{g}}}\right) \right] d\epsilon, \quad (24)$$

where ϵ is the photon energy and F_{C} is the normalization of the Comptonized component. In this regime, repeated Compton scattering leads to a spectral index $p = \ln \tau_T / \ln(1 + A)$ (Rybicki & Lightman 1979; Krolik 1999), and energy conservation and the definition of Θ_{C} can be written as

$$\begin{aligned} \frac{E_{\text{r}}}{t_{\text{esc}}} &= \int_{k_{\text{B}}T_{\text{d}}^-}^{\infty} d\epsilon F(\epsilon) \\ &= (1 - \tau_T)F_{\text{d}} + \Gamma(p + 1, T_{\text{d}}/T_{\text{g}})F_{\text{C}}, \quad (25) \\ 4\Theta_{\text{C}}m_e c^2 &= \frac{\int_{k_{\text{B}}T_{\text{d}}^-}^{\infty} d\epsilon \epsilon F(\epsilon)}{\int_{k_{\text{B}}T_{\text{d}}^-}^{\infty} d\epsilon F(\epsilon)} \\ &= \frac{(1 - \tau_T)(T_{\text{d}}/T_{\text{g}})F_{\text{d}} + \Gamma(p + 2, T_{\text{d}}/T_{\text{g}})F_{\text{C}}}{(1 - \tau_T)F_{\text{d}} + \Gamma(p + 1, T_{\text{d}}/T_{\text{g}})F_{\text{C}}} k_{\text{B}}T_{\text{g}}, \quad (26) \end{aligned}$$

with Γ the incomplete gamma function. Solving these equations yields F_{C} and Θ_{C} ; in case $F_{\text{C}} < 0$, we set $\Theta_{\text{C}} = 0$.

If $\tau_T \geq 1/e$, we assume every photon is scattered at least once on its way out, so we retain only the Comptonized component:

$$F(\epsilon) d\epsilon = \frac{F_{\text{C}}}{k_{\text{B}}T_{\text{g}}} \left(\frac{\epsilon}{k_{\text{B}}T_{\text{g}}} \right)^p \exp\left(-\frac{\epsilon}{k_{\text{B}}T_{\text{g}}}\right) d\epsilon. \quad (27)$$

The spectral parameters F_{C} , p , and Θ_{C} are determined in this regime from photon conservation, energy conservation, and the definition of Θ_{C} :

$$\frac{F_{\text{d}}}{k_{\text{B}}T_{\text{d}}} = \int_{k_{\text{B}}T_{\text{d}}}^{\infty} d\epsilon \epsilon^{-1} F(\epsilon) = \Gamma(p, T_{\text{d}}/T_{\text{g}}) \frac{F_{\text{C}}}{k_{\text{B}}T_{\text{g}}}, \quad (28)$$

$$\frac{E_{\text{r}}}{t_{\text{esc}}} = \int_{k_{\text{B}}T_{\text{d}}}^{\infty} d\epsilon F(\epsilon) = \Gamma(p + 1, T_{\text{d}}/T_{\text{g}})F_{\text{C}}, \quad (29)$$

$$4\Theta_{\text{C}}m_e c^2 = \frac{\int_{k_{\text{B}}T_{\text{d}}}^{\infty} d\epsilon \epsilon F(\epsilon)}{\int_{k_{\text{B}}T_{\text{d}}}^{\infty} d\epsilon F(\epsilon)} = \frac{\Gamma(p + 2, T_{\text{d}}/T_{\text{g}})}{\Gamma(p + 1, T_{\text{d}}/T_{\text{g}})} k_{\text{B}}T_{\text{g}}. \quad (30)$$

5.3. Solution

Figure 6 shows one solution of the model; other solutions are qualitatively similar, differing only in the durations of the various stages of evolution. The first stage is so optically thin that $(A - 4\Theta_{\text{C}})t_{\text{esc}}/t_{\text{sca}} = (A - 4\Theta_{\text{C}})\tau_T m_{\text{H}} / (2\bar{m}) \ll 1$; thus, the net amplification of the disk emission is small. The third term on the right-hand side of Equation (9) largely offsets the first term, so E_{r} grows slowly and T_{g} remains high. Indeed,

$$E_{\text{g}} \approx \langle \rho_f v_{f,z} K \rangle t, \quad (31)$$

$$E_{\text{r}} \approx F_{\text{d}} t / (1 + c/v_{\text{sh}}), \quad (32)$$

$$E_{\infty} \approx F_{\text{d}} t. \quad (33)$$

The second stage commences when $(A - 4\Theta_{\text{C}})t_{\text{esc}}/t_{\text{sca}} = (A - 4\Theta_{\text{C}})\tau_T m_{\text{H}} / (2\bar{m}) \sim 1$. Although the column is still Compton-thin, the scattered photons gain so much energy that the luminosity of a cohort of injected photons is at least doubled. This drives up E_{r} , which in turn accelerates Compton cooling, resulting in an exponential surge in E_{r} . The oscillations in this stage are due to the mutual feedback between E_{g} and E_{r} in our model, in which a column evolves independently of its neighbors; if adjacent columns interacted by photon diffusion, these oscillations would likely be damped.

The growth of E_{r} comes to an end when the system finds a new equilibrium. In this equilibrium, dissipated energy is efficiently converted to radiation energy, which in turn is lost rapidly to outward streaming. This means the two terms of Equation (8) are comparable, while the second term of Equation (9) is counteracted by the third. The effective temperature of the emergent radiation is then

$$T_{\text{eff}} = \left(\frac{E_{\text{r}}}{t_{\text{esc}}\sigma_{\text{SB}}} \right)^{1/4} \sim \left(\frac{\langle \rho_f v_{f,z} K \rangle}{\sigma_{\text{SB}}} \right)^{1/4}. \quad (34)$$

The third stage goes from the moment when $\tau_T \sim 1$, should it happen, to the end of deposition. Compton cooling is faster in the Compton-thick column, but the gas is kept warm by continual energy dissipation. The balance of terms is the same as in the second stage; hence, $(A - 4\Theta_{\text{C}})t_{\text{esc}}/t_{\text{sca}} = (A - 4\Theta_{\text{C}})\tau_T^2 m_{\text{H}} / (2\bar{m}) \sim 1$. The close match between dissipative gains and radiative losses

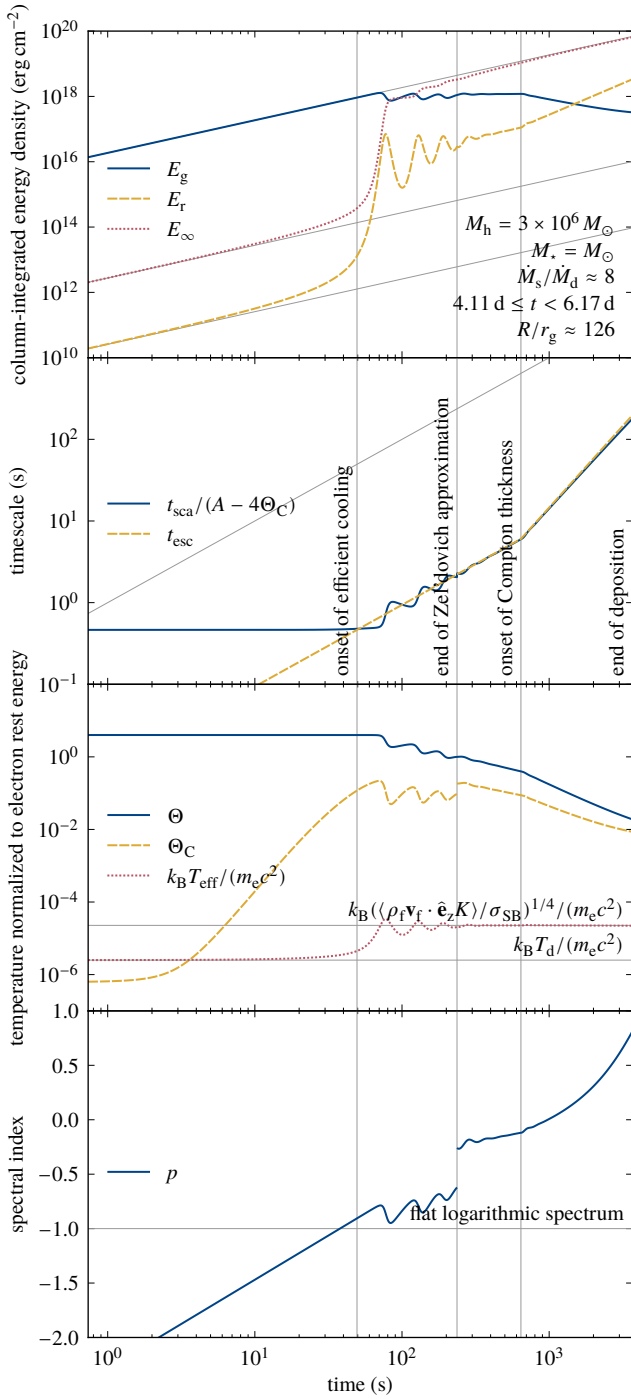


Figure 6. One solution of the cooling model; see §5.2 for definitions. The vertical lines from left to right mark the times when $(A - 4\Theta_C)t_{\text{esc}}/t_{\text{sca}} = 1$, $\tau_T = 1/e$, and $\tau_T = 1$, respectively; the first two times may be interchanged in other solutions. The inclined lines in the first panel are given by Equations (31)–(33). The inclined line in the second panel follows a one-to-one ratio.

means that, once deposition ceases, the gas promptly cools off and little further emission occurs.

Because all quantities as functions of time are approximately power-law, later stages of cooling tend to outweigh earlier stages in terms of contribution to the overall radiative output.

On the whole, both p and Θ_C increase over time in all three stages as long as material continues to be deposited, but p never

rises to above 3, its value in the Rayleigh–Jeans limit. By contrast, Θ is almost constant in the first stage, but falls gradually in the next two stages, bounded below by Θ_C . This observation can be further generalized: a Compton-thicker layer tends to have a larger p and a smaller Θ . Consequently, the spectrum emerging from the column transforms from a soft power law with a high-energy cutoff to a hard power law with a low-energy cutoff as cooling progresses.

Free–free cooling is more efficient for small M_h , large M_* , and large R/r_p . It can be orders of magnitude faster than Compton cooling at converting E_g to E_r in the first phase, but for most of the cases we considered, Compton cooling quickly catches up in the second and third phases, and even monopolizes the cooling budget toward the end of deposition. Therefore, the effect of early-time free–free cooling is likely limited to creating extra seed photons for Compton cooling. Free–free cooling can also dominate after the end of deposition; however, in most cases only a small fraction of the total dissipated energy remains in the column by the time stream material stops arriving, so the contribution of late-time free–free cooling is minor.

Another source of seed photons is the disk interior to the first impact, which could be emitting at Eddington levels (Chan et al. 2019, 2020). Although this could, in principle, be a competitive source of seed photons, the luminosity and angular distribution of this light remain so uncertain that we do not include it here.

5.4. Spectra and luminosities

The analysis so far concerns a single column. Figure 7 shows the overall spectra resulting from the second impact for various values of M_h and M_* . These are obtained by adding together the contribution of every column on the disk. In all cases, it can be roughly represented by a broken power law whose break coincides with the peak in ϵL_ϵ . Depending on M_h and M_* , the photon energy of the peak can be anywhere between ~ 10 keV and 1 MeV, as expected from Compton cooling of mildly relativistic electrons. Generally speaking, with increasing M_h and decreasing M_* , the peak broadens and shifts toward higher energies. Additional cooling at $t \geq t_{\text{dep}}$ modifies the spectrum, the most prominent effect being the creation of a secondary \sim keV peak for small M_h and large M_* .

The spectra in Figure 7 have bolometric luminosities ranging from $\sim 10^{42}$ to 10^{44} erg s $^{-1}$, on the level of weak AGNs. Because the shocked material cools efficiently, these luminosities are close to the total energy dissipation rate, which is $\sim 0.2 \dot{M}_s$ times the specific kinetic energy of the disk at the second impact (§4.2). Second-impact radii are multiples of r_p , so the luminosity scales as

$$L \propto GM_h \dot{M}_s / r_p \propto M_h^{1/6} M_*^{7/3} r_*^{-5/2} \Psi^{-1} \Xi^{3/2} \propto M_h^{1/6} M_*^{0.13} \Psi^{-1} \Xi^{3/2}. \quad (35)$$

As seen in Figure 8, this equation best describes the luminosities from the model when the constant associated with the first proportionality is $\sim 4 \times 10^{-3}$:

$$L \sim 1.8 \times 10^{43} \text{ erg s}^{-1} \times \Psi^{-1} \Xi^{3/2} \left(\frac{M_h}{3 \times 10^6 M_\odot} \right)^{1/6} \left(\frac{M_*}{M_\odot} \right)^{0.13}. \quad (36)$$

The proportionality constant is so small because merely $\sim 20\%$ of the bound debris participates in the second impact, and because,

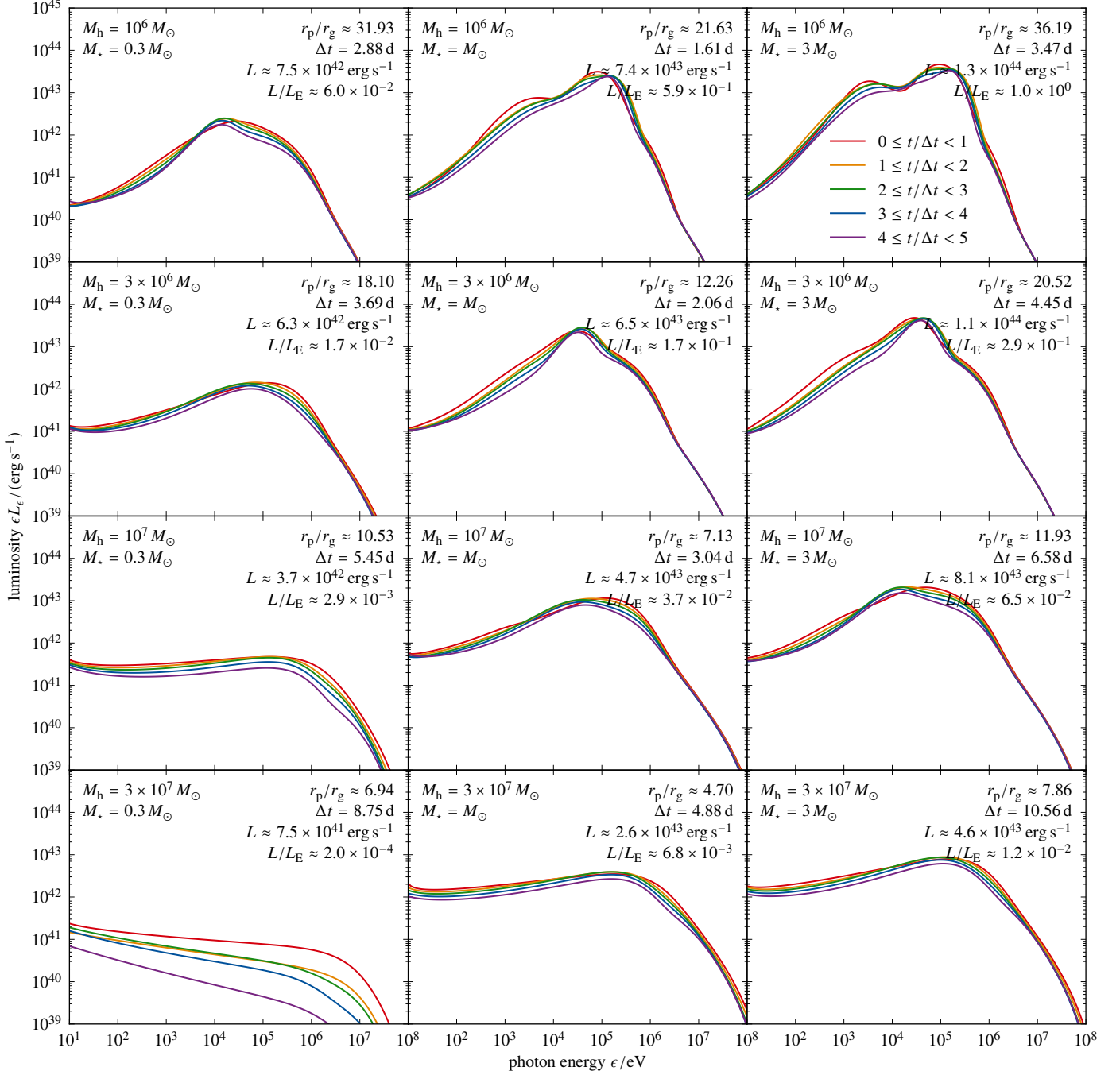


Figure 7. Disk-integrated second-impact spectra for $\dot{M}_s/\dot{M}_d \approx 8$. All panels share the same legend, but the value of $\Delta t = 280 (GM_h/r_p^3)^{-1/2}$ varies from panel to panel. Here $L_E = 4\pi GM_h c m_H / \sigma_T$ is the Eddington luminosity.

according to Figure 3, the second impact happens at several tens of r_p .

In view of the weak “nominal” dependence of L on M_h and M_\star , the correction factors Ψ and Ξ actually control how L scales with M_h and M_\star . The combination $\Psi^{-1}\Xi^{3/2}$ decreases with M_h and increases with M_\star , counteracting the nominal M_h -dependence but augmenting the nominal M_\star -dependence. As is apparent from Figures 7 and 8, L is most sensitive to M_h for $M_h \gtrsim 3 \times 10^6 M_\odot$, and to M_\star for $0.1 M_\odot \lesssim M_\star \lesssim M_\odot$.

6. DISCUSSION

6.1. Identifying second-impact signatures in TDE searches

TDEs in AGNs have observational signatures that are emphatically unlike TDEs in vacuum. They do not have optical/UV light curves that follow the mass-return rate, as is commonly expected for their vacuum counterparts (e.g., Rees 1988). Instead, the destruction of the inner disk by the first impact sustains an Eddington-level luminosity plateau over tens of days (Chan et al. 2019, 2020). On top of that, the second impact begets a longer-lasting signal whose

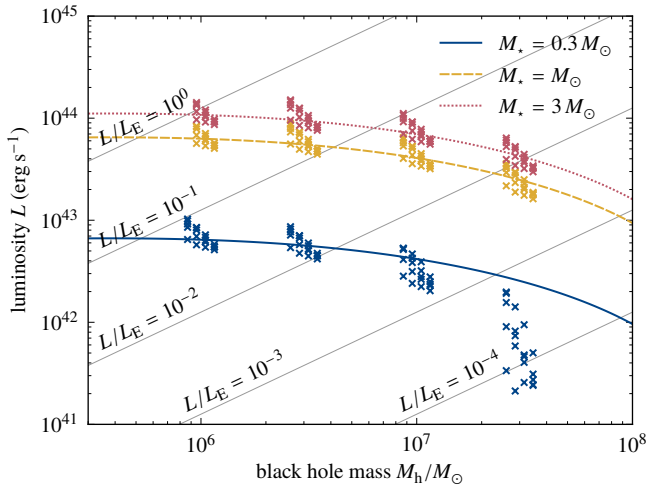


Figure 8. Luminosity of the second impact. The crosses are the luminosities predicted by our cooling model; there is one cross for every \dot{M}_s/\dot{M}_d and for every one-fifth of the simulation duration (§5.1). For clarity, the crosses are displaced horizontally by a small amount according to their \dot{M}_s/\dot{M}_d , with \dot{M}_s/\dot{M}_d increasing from left to right. The luminosity depends weakly on \dot{M}_s/\dot{M}_d and time in most cases. The curves are given by Equation (36). That equation estimates the second-impact luminosity to be equal to its characteristic energy dissipation rate, and the overall normalization of the estimate is chosen to fit the model luminosities. The goodness of the fit suggests that the material shocked at the second impact cools efficiently.

luminosity does follow the mass-return rate thanks to efficient cooling, but its typical photon energy is not in the optical/UV: most of the spectra in Figure 7 peak between ~ 10 keV and 1 MeV. Such spectra bear no resemblance to the tens-of-eV thermal spectrum originally expected from the accretion disk formed by TDEs in vacuum (Cannizzo et al. 1990; Ulmer 1999) and is sometimes observed in soft X-ray TDEs (see Saxton et al. 2020 for a review).

The hard second-impact spectrum could mean that TDE searches focused on softer spectra would miss it altogether. The hunt is made difficult by the fact that, unlike jetted TDEs with isotropic-equivalent X-ray luminosities of $\sim 10^{46}$ to 10^{48} erg s $^{-1}$ (Bloom et al. 2011; Burrows et al. 2011; Levan et al. 2011; Cenko et al. 2012), the second impact emits at rates four orders of magnitude lower.

6.2. Second-impact signatures versus AGN variability

Another challenge in the identification of second-impact signatures is distinguishing them from common AGN variability. Two aspects may provide the means to do so: spectral hardness and pattern of time variation.

The second impact has much harder spectra than ordinary AGNs. The coronal component of unobscured AGN spectra typically has $-1 \lesssim d \log L_\epsilon / d \log \epsilon \lesssim -0.7$ from ~ 1 to 100 keV (e.g., Liu et al. 2016; Ricci et al. 2017). Judging by Figure 7, the X-rays from the second impact should have $-1 \lesssim d \log L_\epsilon / d \log \epsilon \lesssim 0$. The contrast between unobscured AGN spectra and the significantly harder second-impact spectra is enhanced to the degree that the corona is disrupted by the first impact, an outcome suggested in our earlier work (Chan et al. 2019; Ricci et al. 2020).

In addition to unobscured AGNs, there is also a roughly

comparable number of obscured AGNs (e.g., Huchra & Burg 1992; Reyes et al. 2008; Brightman & Nandra 2011; Wilkes et al. 2013; Oh et al. 2015). Our sightlines to these AGNs are obscured by neutral gas with hydrogen column densities N_H of $\sim 10^{22}$ to 10^{24} cm $^{-2}$ or more. A column with $N_H \sim 10^{22}$ cm $^{-2}$ absorbs essentially all photons below ~ 2 keV, and one with $N_H \sim 10^{24}$ cm $^{-2}$ absorbs all photons under ~ 7 to 10 keV. A column with still higher N_H scatters all photons with energies up to $\gtrsim 100$ keV. A significant fraction of all obscured AGNs, from ~ 20 to 50%, may belong to this last category (Ricci et al. 2015; Georgantopoulos & Akylas 2019; Kammoun et al. 2020). Because this obscuration is mostly located parsecs away from the black hole, if it blocks X-rays from an AGN, it will equally block those due to a TDE. The only photons we can see are relatively high-energy, which makes the contrast between the second impact and the unperturbed AGN especially high.

The smooth brightening and fading of the second impact could provide another method of distinction. The X-ray light curves of normal AGNs generically exhibit “red noise,” that is, their Fourier power spectra are power laws declining from timescales of months or years to timescales of hours (e.g., Lawrence et al. 1987; McHardy & Czerny 1987; Lawrence & Papadakis 1993), and individual modes of the power spectra have little or no phase coherence (Krolik et al. 1993). By contrast, the second impact should brighten and fade smoothly over a period of months, in response to the variation of the mass-return rate. The existence of a dominant timescale, and the phase coherence implied by the smoothness of the light curve, may help make a second-impact flare distinct.

6.3. Caveats about second-impact signatures

Our treatment of light production at the second impact depends on a number of approximations and simplifications. A few warrant identification as possible starting points for future improvements.

The simulations underlying our cooling model injected the stream on a parabolic orbit (Chan et al. 2019) when, in fact, the debris is weakly bound. Therefore, the stream’s kinetic energy at pericenter is overestimated by an amount comparable to its typical binding energy. After correcting for this offset, the second impact would happen at smaller radii. This would increase the energy dissipated per unit stream mass somewhat, raise the luminosity, and change the spectrum. A greater fraction of the stream could also end up in the second impact, making the cooling emission from it softer and more thermal (§5.3).

As in Chan et al. (2019, 2020), we consider here a specific stream configuration: the stream hits the disk perpendicularly while passing through its pericenter at radius \mathcal{R}_t . Our results might change depending on stream orientation and pericenter, but preliminary estimates suggest that orientation does not qualitatively affect our conclusions.

Our model ignores the production of electron–positron pairs for simplicity (§5.2), but many pairs should be produced in the freshly shocked gas with temperatures $k_B T_g \gtrsim m_e c^2$. In pair equilibrium, some of the thermal energy is held in the rest mass of pairs, while pair annihilation adds to the number density of photons. The increase in scattering opacity due to pairs combined with the presence of additional photons tends to promote lower gas and radiation temperatures, and more nearly thermal spectra.

Lastly, our simulations cover merely a fraction of the mass-return time, during which the stream mass current can be taken to be approximately constant. However, as the mass-return rate rises, reaches a peak, and then falls over the course of the TDE, we expect the bolometric luminosity of the second impact to roughly track that rate, while the spectrum should evolve from harder at the initially low mass-return rate, to softer and more thermal near the peak, and then back to harder as the mass-return rate decays.

7. CONCLUSIONS

As argued in Chan et al. (2019), some fraction of all TDEs should take place in AGNs. These TDEs have drastically different physics and phenomenology from those in inactive galaxies due to the pre-existing AGN disk. The disk does not affect the disruption, but it can block the returning debris stream. The dynamics and observational properties of these TDEs are thus defined by the multiple interactions between the stream and the disk. The mechanisms commonly considered in connection with TDEs in vacuum cannot be applied to TDEs in AGNs, and they certainly cannot explain any optical/UV emission from the latter.

For TDEs in AGNs, the first impact of the stream with the disk takes place near stream pericenter. The shocks generated cause the disk interior to the impact point to fall rapidly into the black hole, and they power a short-lived Eddington-limited luminosity plateau (Chan et al. 2019), possibly thermal in spectrum. The plateau lasts tens of days (Chan et al. 2020) if the tidal radius is estimated using an order-of-magnitude estimate (e.g., Rees 1988). Accounting for the effects of general relativity and stellar structure on the disruption changes the duration by a factor of a few (Ryu et al. 2020a); for example, the plateau duration for a Sun-like star disrupted by a $3 \times 10^6 M_{\odot}$ black hole accreting at 0.01 times Eddington is shortened from ~ 10 d to ~ 3 d.

In most cases, a large fraction of the stream drives through the disk at the first impact, only to encounter the disk again at larger distances. The stream is stopped at this second impact and heated to temperatures ~ 100 keV. Compton cooling produces hard X-rays to soft γ -rays with a strikingly hard spectrum: most of the energy is carried by photons from ~ 10 keV to 1 MeV. The luminosity tracks the mass-return rate, reaching $\sim 10^{42}$ to 10^{44} erg s^{-1} at peak; this means the timescale of the light curve is roughly a few months. The spectrum is harder when the luminosity is low, and softer and more thermal when the luminosity is high.

Second-impact emission may be distinguished from intrinsic AGN light by its exceptionally hard spectrum, and the smooth time variation of its luminosity roughly following the mass-return rate. If the first impact disrupts the inner disk's corona (Chan et al. 2019; Ricci et al. 2020), then the few-keV coronal emission of the normal AGN would be reduced, and the tens-of-keV second-impact radiation would stand out even more.

A third source of radiation not discussed here arises from the unbound debris interacting with the circumnuclear environment; such debris can be unbound either during the disruption (Krolik et al. 2016; Yalinewich et al. 2019), or by a boost from the disk at the first impact (Chan et al. 2019). Synchrotron radiation, similar to that of supernova remnants, would be produced at the shocks generated by the outflowing debris. Such radio signatures have been observed in TDEs such as ASASSN-14li (Alexander

et al. 2016; van Velzen et al. 2016; Bright et al. 2018). TDEs are expected to produce stronger radio emission in AGNs because of the higher circumnuclear densities.

Finally, by severely disturbing the disk, a TDE can leave an enduring mark on an AGN. The AGN accretion rate may be enhanced for years to come because half a star has been deposited in the disk. Alternatively, the accretion rate may be reduced after the end of the TDE because the first impact has emptied the inner disk into the black hole.

To summarize, TDEs in AGNs are expected to show a bolometric luminosity plateau extending for tens of days. This is followed by ~ 10 keV to 1 MeV hard X-rays and soft γ -rays that track the mass-return rate; the typical photon energy is much harder than in non-jetted TDEs, and the observed luminosity is several orders of magnitude below jetted TDEs. At the same time, the debris unbound during the disruption and at the first impact can interact with the circumnuclear gas and produce synchrotron radiation much brighter than TDEs in vacuum.

CHC and TP were partially supported by ERC advanced grant ‘‘TREx.’’ JHK was partially supported by NSF grant AST-1715032.

Software: Athena++ (Stone et al. 2020), NumPy (Harris et al. 2020), Matplotlib (Hunter 2007)

REFERENCES

- Alexander, K. D., Berger, E., Guillochon, J., Zauderer, B. A., & Williams, P. K. G. 2016, *ApJL*, **819**, L25
- Auchettl, K., Ramirez-Ruiz, E., & Guillochon, J. 2018, *ApJ*, **852**, 37
- Bloom, J. S., Giannios, D., Metzger, B. D., et al. 2011, *Sci*, **333**, 203
- Bright, J. S., Fender, R. P., Motta, S. E., et al. 2018, *MNRAS*, **475**, 4011
- Brightman, M., & Nandra, K. 2011, *MNRAS*, **414**, 3084
- Burrows, D. N., Kennea, J. A., Ghisellini, G., et al. 2011, *Natur*, **476**, 421
- Cannizzo, J. K., Lee, H. M., & Goodman, J. 1990, *ApJ*, **351**, 38
- Centeno, S. B., Krimm, H. A., Horesh, A., et al. 2012, *ApJ*, **753**, 77
- Chan, C.-H., Piran, T., & Krolik, J. H. 2020, *ApJ*, **903**, 17
- Chan, C.-H., Piran, T., Krolik, J. H., & Saban, D. 2019, *ApJ*, **881**, 113
- Dai, L., McKinney, J. C., & Miller, M. C. 2015, *ApJL*, **812**, L39
- Frederick, S., Gezari, S., Graham, M. J., et al. 2020, arXiv: 2010.08554
- Georgantopoulos, I., & Akylas, A. 2019, *A&A*, **621**, A28
- Haardt, F., & Maraschi, L. 1991, *ApJL*, **380**, L51
- Harris, C. R., Millman, K. J., van der Walt, S. J., et al. 2020, *Natur*, **585**, 357
- Hills, J. G. 1975, *Natur*, **254**, 295
- Huchra, J., & Burg, R. 1992, *ApJ*, **393**, 90
- Hunter, J. D. 2007, *CSE*, **9**, 90
- Just, A., Yurin, D., Makukov, M., et al. 2012, *ApJ*, **758**, 51
- Kammoun, E. S., Miller, J. M., Koss, M., et al. 2020, *ApJ*, **901**, 161
- Kankare, E., Kotak, R., Mattila, S., et al. 2017, *NatAs*, **1**, 865
- Kochanek, C. S. 1994, *ApJ*, **422**, 508
- Komossa, S. 2015, *JHEAp*, **7**, 148
- Krolik, J., Done, C., & Madejski, G. 1993, *ApJ*, **402**, 432
- Krolik, J., Piran, T., Svirski, G., & Cheng, R. M. 2016, *ApJ*, **827**, 127
- Krolik, J. H. 1999, Active galactic nuclei: From the central black hole to the galactic environment (Princeton, NJ: Princeton University Press)
- Lawrence, A., & Papadakis, I. 1993, *ApJL*, **414**, L85

- Lawrence, A., Watson, M. G., Pounds, K. A., & Elvis, M. 1987, *Natur*, [325](#), 694
- Levan, A. J., Tanvir, N. R., Cenko, S. B., et al. 2011, *Sci*, [333](#), 199
- Liu, Z., Merloni, A., Georgakakis, A., et al. 2016, *MNRAS*, [459](#), 1602
- Loeb, A., & Ulmer, A. 1997, *ApJ*, [489](#), 573
- Lu, W., & Bonnerot, C. 2020, *MNRAS*, [492](#), 686
- MacLeod, M., & Lin, D. N. C. 2020, *ApJ*, [889](#), 94
- Matsumoto, T., & Piran, T. 2021, *MNRAS*, [502](#), 3385
- McHardy, I., & Czerny, B. 1987, *Natur*, [325](#), 696
- Metzger, B. D., & Stone, N. C. 2016, *MNRAS*, [461](#), 948
- Miralda-Escudé, J., & Kollmeier, J. A. 2005, *ApJ*, [619](#), 30
- Oh, K., Yi, S. K., Schawinski, K., et al. 2015, *ApJS*, [219](#), 1
- Piran, T., Svirski, G., Krolik, J., Cheng, R. M., & Shiokawa, H. 2015, *ApJ*, [806](#), 164
- Rauch, K. P. 1995, *MNRAS*, [275](#), 628
- Rees, M. J. 1988, *Natur*, [333](#), 523
- Reyes, R., Zakamska, N. L., Strauss, M. A., et al. 2008, *AJ*, [136](#), 2373
- Ricci, C., Kara, E., Loewenstein, M., et al. 2020, *ApJL*, [898](#), L1
- Ricci, C., Trakhtenbrot, B., Koss, M. J., et al. 2017, *ApJS*, [233](#), 17
- Ricci, C., Ueda, Y., Koss, M. J., et al. 2015, *ApJL*, [815](#), L13
- Rybicki, G. B., & Lightman, A. P. 1979, Radiative processes in astrophysics (New York: John Wiley & Sons)
- Ryu, T., Krolik, J., Piran, T., & Noble, S. C. 2020a, *ApJ*, [904](#), 98
- . 2020b, *ApJ*, [904](#), 99
- Saxton, R., Komossa, S., Auchettl, K., & Jonker, P. G. 2020, *SSRv*, [216](#), 85
- Shakura, N. I., & Sunyaev, R. A. 1973, *A&A*, [24](#), 337
- Shiokawa, H., Krolik, J. H., Cheng, R. M., Piran, T., & Noble, S. C. 2015, *ApJ*, [804](#), 85
- Stone, J. M., Tomida, K., White, C. J., & Felker, K. G. 2020, *ApJS*, [249](#), 4
- Suková, P., Zajaček, M., Witzany, V., & Karas, V. 2021, arXiv: [2102.08135](#)
- Syer, D., Clarke, C. J., & Rees, M. J. 1991, *MNRAS*, [250](#), 505
- Trakhtenbrot, B., Arcavi, I., Ricci, C., et al. 2019, *NatAs*, [3](#), 242
- Ulmer, A. 1999, *ApJ*, [514](#), 180
- Van Velzen, S., Anderson, G. E., Stone, N. C., et al. 2016, *Sci*, [351](#), 62
- Van Velzen, S., Gezari, S., Hammerstein, E., et al. 2021, *ApJ*, [908](#), 4
- Wilkes, B. J., Kuraszkiewicz, J., Haas, M., et al. 2013, *ApJ*, [773](#), 15
- Yalinewich, A., Steinberg, E., Piran, T., & Krolik, J. H. 2019, *MNRAS*, [487](#), 4083